Colloids and Surfaces B: Biointerfaces 193 (2020) 111100

Contents lists available at ScienceDirect

Colloids and Surfaces B: Biointerfaces

journal homepage: www.elsevier.com/locate/colsurfb

Spontaneous collapse of palmitic acid films on an alkaline buffer containing calcium ions

Pin Zhang[a], Tiep Pham[a], Xin Zheng[b], Chang Liu[a], Paola Leon Plata[a], Petr Král[a,b,c,d], Wei Bu[e], Binhua Lin[e], Ying Liu[a,d,f,*]

[a] Department of Chemical Engineering, University of Illinois at Chicago, Chicago, IL 60608, United States
[b] Department of Chemistry, University of Illinois at Chicago, Chicago, IL 60607, United States
[c] Department of Physics, University of Illinois at Chicago, Chicago, IL 60607, United States
[d] Department of Biopharmaceutical Sciences, University of Illinois at Chicago, Chicago, IL 60607, United States
[e] NSF's ChemMatCARS, University of Chicago, IL 60637, United States
[f] Department of Bioengineering, University of Illinois at Chicago, Chicago, IL 60607, United States

ARTICLE INFO

Keywords:
Self assembly
Inverted bilayer
Superstructure
Langmuir trough
Synchrotron X-ray
Reflectivity
Diffraction
Nucleation and growth
Electrostatic interactions
Constant surface area

ABSTRACT

Understanding the interaction of ions with fatty acids is important to identify their roles in various bioprocesses and to build novel biomimetic systems. In this study, the molecular organization of palmitic acid (PA) films on alkaline buffer solutions (pH 7.4) with and without divalent Ca^{2+} was measured at a constant surface area using Langmuir troughs coupled with microscopy and X-ray interfacial techniques. Without Ca^{2+}, PA molecules remained a monolayer organization; however, with Ca^{2+}, formation of the inverted bilayers of PA-Ca^{2+} superstructures caused a spontaneous 2D to 3D transformation under no compression due to the strong interaction between PA and the divalent cation. Self-assembly of this highly-organized inverted bilayer superstructure involved a two-step process of nucleation and nuclei growth. During nucleation, densely packed PA and Ca^{2+} monolayer firstly corrugated and some of PA and Ca^{2+} molecules ejected out from the monolayer; the ejected molecules then reorganized and formed the inverted bilayer nuclei. Nucleation was followed by nuclei growth, during which PA and Ca^{2+} in the monolayer kept integrating into the inverted bilayer structure through molecule migration and PA rotation around Ca^{2+}.

1. Introduction

Fatty acids are an important energy source and a major component of dietary fats and cell membranes. [1] The interaction between fatty acids and ions is central to many biological processes such as ion transport through membranes and mineralization of biological assemblies [2–4]. Langmuir monolayers of fatty acids and lipids as model systems have been used to study membrane behaviors. The electrostatic interactions of saturated fatty acids (SFA) with cations, particularly divalent or multivalent cations, are responsible for the formation of highly organized superstructures [5–7]. We therefore investigated the spontaneous film reorganization of palmitic acid (PA), one of the most common fatty acids in the daily diet, with Ca^{2+} at a constant surface area with a very low surface pressure. The superstructure of palmitic acid and cations contributes significantly to lipid rafts, which are the microdomains of plasma membranes that act as cell signaling platform and have been reported to be essential for modulating cholesterol, ion transport, and lipoprotein assembly, secretion, and clearance, etc.

Without cations, the films of fatty acids generally undergo a collapsing process at a constant compression pressure when the surface pressure goes beyond the critical pressures. However, when the interactions of fatty acids and cations in the subphase are sufficiently strong, the film collapse could happen at a low surface pressure. For example, cation-induced stearic acid monolayer collapse has been observed at a low pressure, [8,9] and the spontaneous formation of the Cd^{2+}-behenic acid (BA) superlattice structures has been reported. [10]

The molecular processes of SFA film collapse on buffers containing divalent cations depend on the electrostatic interaction between the cations and the acidic head groups of SFAs and the lipophilic interactions between the alkyl tails, which can be varied by changing the experimental parameters, such as fatty acid tail length, buffer pH value, cation concentration, and types of divalent cations involved. [11] In general, when the electrostatic interaction of the cations with the SFAs is weak, the cations only condense the packing of the SFA molecules,

* Corresponding author.
E-mail address: liuying@uic.edu (Y. Liu).

https://doi.org/10.1016/j.colsurfb.2020.111100
Received 26 January 2020; Received in revised form 27 April 2020; Accepted 28 April 2020
Available online 06 May 2020

and a high surface pressure is required for the film to collapse [4,12–14]. In this case, two possible results may follow the film collapse: a rigid film breaks up into multiple-layer fragments in four successive steps of weakening, folding, bending, and breaking [15], while the collapse of a fluid film causes loss of material from the film into the subphase through either molecular dissolution or formation of lipid aggregates such as vesicles or micelles [16,17]. In contrast, when the electrostatic interaction of the cations with the SFAs is strong, such as in conditions of high pH [18], abundant divalent cations [19], low temperature [3,20], or high ionic strength [21], formation of SFA–divalent cation superstructures (in which cations generate ordered layers) might happen at a low constant compressing pressure [7,19,22]. A nucleation-growth collision theory has been proposed to describe the growth kinetics of 3-D structures from supersaturated monolayers under a low continuous compression [23,24]. However, for the spontaneous collapse of an SFA film in the presence of divalent cations at a constant area without compression, the mechanism remains unclear. Here, we propose that the nucleation is caused by surface corrugation and PA ejection and the growth is mainly contributed by molecular transport of PA and Ca^{2+} from the monolayer phase to the inverted bilayer phase and PA rotation around Ca^{2+}.

It has been reported that divalent cations such as Ca^{2+} are unable to form superstructures with SFAs; [8,25] however, we observed formation of PA-Ca^{2+} superstructures on a pH 7.4 buffer with 5 mM Ca^{2+} [5,6]. As Ca^{2+} is one of the most important and abundant divalent ions involved in diverse biological signaling processes and assemblies, examination of its interaction with SFAs is necessary to advance our understanding of the biological roles of Ca^{2+}. Moreover, the spontaneous reorganization phenomenon and the associated mechanism may be used to design biomimetic systems.

In this study, we performed *in situ* measurements of the spontaneous collapse kinetics of PA films over time at a constant surface area on a buffer containing 5 mM Ca^{2+} with a physiological pH value of 7.4. The area-pressure isotherms and topographies of PA films were monitored using a Langmuir trough integrated with fluorescence microscopy. The film molecular packing structures in both horizontal and perpendicular directions were quantified by combining the results of X-ray reflectivity (XR) and grazing incidence X-ray diffraction (GIXD). The interfacial organization of PA films on the same alkaline buffer without Ca^{2+} was also measured as a comparison. Finally, to reveal the critical steps that lead to the reorganization of the PA-Ca^{2+} films, molecular dynamics (MD) simulations were conducted.

2. Experimental

2.1. Materials and reagents

PA, tris-base, calcium chloride dihydrate, and hydrochloric acid as well as all organic solvents, including methanol, ethanol, and chloroform, were purchased from Sigma-Aldrich. A lipid conjugated with a fluorescent dye, 1,2-dipalmitoyl-sn-glycero-3-phosphoethanolamine-N-(lissamine rhodamine B sulfonyl) (DPPE-Rhod, Ex/Em 560 nm/583 nm) was purchased from Avanti Polar Lipids. Two types of subphase buffer solutions with and without Ca^{2+} were used in the study. The Ca buffer contained 5 mM $CaCl_2$ and 8 mM tris, while the Ca-free buffer consisted of 8 mM tris only. The pH of both buffers was adjusted to 7.4 by adding diluted hydrochloric acid. The solutions were degassed under vacuum for 3 h before the measurements to reduce oxygen, during which the volume change by evaporation was negligible and the change in Ca^{2+} concentration was less than 1%. Water used in all experiments was deionized to 18.2 MΩ (MILLIPORE). All chemicals were purchased at standard grades and were used as received.

2.2. Isotherm and topography measurement

A Langmuir trough (51 × 155 mm^2, Biolin Scientific) mounted under an inverted fluorescence microscope (Observer D1-AX10, Zeiss) was used to monitor the topography and surface pressure changes of the PA films at the gas-liquid interface while the films were maintained at a constant surface area. The fluorescence microscope was equipped with a 20 × objective (LD Plan-NEOFLUAR, Zeiss), and the incident light was provided by an X-Cite series 120 Q bulb with a TEXAS RED filter (Ex 565 nm/Em620 nm). The surface pressure was monitored using a platinum Wilhelmy plate attached to an electronic balance.

Before each experiment, the trough was cleaned thoroughly, which was confirmed by a surface pressure variation of less than 0.2 mN/m when the barrier was moved to its entire extent over the gas-liquid interface. The trough was then filled with 55 mL subphase buffer. To provide a fluorescence contrast, 0.5 mol% DPPE-Rhod was premixed with PA in chloroform. With the position of the barriers being fixed, the sample was deposited dropwise on the subphase until the average area per molecule reached 20.6 ± 0.1 $Å^2$. Recording of surface pressure and topography change of the film began immediately and continued for 2 h. During the measurements, the temperature of the subphase was maintained at 23 ± 0.5 °C by a water circulation system (Anova Scientific).

2.3. X-ray measurements

XR and GIXD measurements on the films were conducted at the National Science Foundation's (NSF) ChemMatCARS (15-ID-C) of Advanced Photon Source at Argonne National Laboratory. The X-ray wavelength used in the study was 1.24 Å. All experiments were conducted at about 22.7 °C. A customized Teflon trough (78 × 177.6 mm^2) with a one-side barrier was placed in a box that was integrated within the path of the X-ray beamline. Surface pressure was monitored using a Wilhelmy paper plate hung on an electronic balance. Details of the experimental setup were described in our previous study. [5,6,26]

PA film preparation at the gas-lipid interface was similar to the process described in the previous section. With the position of the barrier being fixed, the PA sample was slowly deposed at the interface until the average area per PA molecule reached 20.6 ± 0.1 $Å^2$, which is consistent with the microscopy experiments. The box containing the trough was then sealed and purged with helium for 20 min to allow solvent evaporation and reduce oxygen level below 2%.

2.4. XR and GIXD data fitting

XR provides information on molecular organization of the film across the interface. As the incident angle was varied, the X-ray reflectivity intensity (R) was recorded by an area detector (Pilatus 100 K) at the reflected angles, which was normalized by the Fresnel reflectivity (R_F). The normalized reflectivity (R/R_F) was fitted using a box model. For PA films on the Ca-free buffer, a single-phase box model was used; for PA films on the Ca buffer, a multi-phase box model was used with incoherent addition of reflectivity from different phases as follows, [27]

$$R_{Incoherent} = \sum C_j * R_j \quad (1)$$

where C_j is the surface coverage of the jth phase, as $\Sigma C_j = 1$, and R_j is the reflectivity intensity of the jth phase.

The electron density (ED) profile for each phase was a sum of error functions,

$$\rho(z) = \frac{1}{2}\sum_{i=0}^{N} erf\left(\frac{z - z_i}{\sqrt{2}\sigma}\right) \times (\rho_i - \rho_{i+1}) + \frac{\rho_0}{2} \quad (2)$$

where N is the number of slabs; z_i is the position of the ith slab; ρ_i is the ED of the ith slab; ρ_0 is the ED of the subphase; and σ is the roughness of the interface. In accordance with the Parratt formalism, [28] parameters were obtained by fitting the experimental results of XR based on nonlinear least-squares analysis.

GIXD measurements probe the crystal structures of the films at the interface. By varying the horizontal wave vector Q_{xy} (horizontal to the

interface) and vertical wave vector Q_z (perpendicular to the interface), the scattered X-ray intensities were recorded. Bragg peaks and Bragg rods were obtained by integrating the GIXD intensities over Q_z and Q_{xy}, respectively. The Bragg peaks were fitted using Gaussian functions, while the Bragg rods were fitted using the distorted wave Born approximation (DWBA). [13]

2.5. MD simulation

MD simulation were performed using Nanoscale Molecular Dynamics (NAMD), [29] with the Chemistry at Harvard Macromolecular Mechanics27 (CHARMM) force field for PA, [30,31] the TIP3P model for water [32], and the CHARMM36 force field for molecular interactions [33,34]. Nonbonded van der Waals interactions were modeled using the Lennard-Jones potential, and the electrostatic interactions were described by a Coulomb potential. The switching distance for interatomic contacts was 10 Å. The cutoff distance between pairs of atoms for electrostatic and van der Waals interactions was 12 Å. The time step was 1 fs. A Langevin dynamics damping coefficient of 5 ps^{-1} was applied to the first nanosecond of equilibration and a damping coefficient of 1 ps^{-1} was applied to the rest. The Particle Mesh Ewald algorithm [35] with a grid spacing of 1 Å accounting for the full electrostatic interactions was employed to reduce computational complexity. A canonical constant-temperature and constant-volume ensemble (NVT, T = 300 K) was used with periodic boundary conditions in all directions. The periodic boundary in the z direction, which is normal to the interface, was lengthened beyond the boundaries of the lipid-water system in order to simulate the liquid-gas boundary while providing x- and y-direction surface-tension-like control.

3. Results and discussion

3.1. Topographies and molecular organization of PA films on Ca and Ca-free buffers

After the PA films were deposited on the Ca and Ca-free buffers, the surface pressure quickly decreased to about 5 mN/m within the first 20 min and then slowly decreased to about 2 mN/m in the following 100 min (Figure s1 in Supplemental Information). During the entire two-hour experimental observation, the interfacial topography of the PA film on the Ca-free buffer remained similar. Specifically, the PA film on the Ca-free buffer consistently contained uniformly distributed, rounded bright domains and a black surrounding phase (Fig. 1A). The brightness was provided by the accumulated DPPE-Rhod molecules. The migration of domains was slow, indicating that the entire interface was covered by the PA film. Therefore, the phase that appeared dark was more likely a condensed phase of ordered PA molecules that excluded DPPE-Rhod molecules rather than a gaseous phase. The bright domains were disorderedly packed PA molecules where DPPE-Rhod molecules tend to be present. Therefore, throughout the entire experiment, the PA film on the Ca-free buffer remained as a mixture of disordered and ordered phases (Fig. 1A).

The topography evolution of the PA film on the Ca buffer was more complicated. Over time, three phases with different levels of fluorescent intensities were observed (Fig. 1B): (1) the initial small bright spots grew into bigger domains, which had the highest fluorescent intensity (marked as 1 in Fig. 1B); (2) the initial continuous dark mottled phase dispersed into domains, which had the intermediate fluorescent intensity (marked as 2 in Fig. 1B); and (3) a uniformly dark surrounding black phase emerged (marked as 3 in Fig. 1B). The brightest domains were likely the inverted bilayer structures of PA-Ca^{2+} complexes. [5] The enrichment of DPPE-Rhod molecules in these domains may be due to the electrostatic interactions between the negatively charged fluorescent dye and the accumulated Ca^{2+} in the inverted bilayer domains. These domains formed quickly after PA was spread on the Ca buffer and kept growing. Domain migration was much faster than that on the Ca-free buffer, indicating that the continuous dark phase (marked as 3 in Fig. 1B) was the gaseous phase. The domains marked as 2 in Fig. 1B might possess a monolayer structure.

While fluorescence microscopy provides direct observations of the film topography evolutions, it is difficult to quantitatively analyze the kinetics of the monolayer, inverted bilayer and gaseous phase transition by using microscopy because of the limited and fixed observation area, and fast drifting of the domains. Therefore, XR and GIXD measurements were carried out to reveal the molecular packing structures of the films and phase transition kinetics.

GIXD measurements reveal the lateral molecular packing structures. For the PA film on the Ca-free buffer, the Bragg peaks (Fig. 2A frame a and Fig. 2B curve a) indicate a nearest-neighbor (NN) packing structure similar to that of the PA film on pure water (at 15 mN/m and 30 °C) [36] with a unit area of 22.6 $Å^2$ and a tilt angle of 25.2° (Fig. 2C, schematic a). Throughout the entire experiment, the GIXD Bragg peaks remained unchanged, indicating an unchanged packing structure over time. For the PA film on the Ca buffer, the GIXD patterns changed significantly overtime. After 20 min of PA deposition, a dominant in-plane GIXD peak appeared at 1.514 $Å^{-1}$ along with two very weak peaks at about 1.41 and 1.84 $Å^{-1}$ (Fig. 2A frame b and Fig. 2B curve b). The strong in-plane Bragg peak at 1.514 $Å^{-1}$ indicates a hexagonal

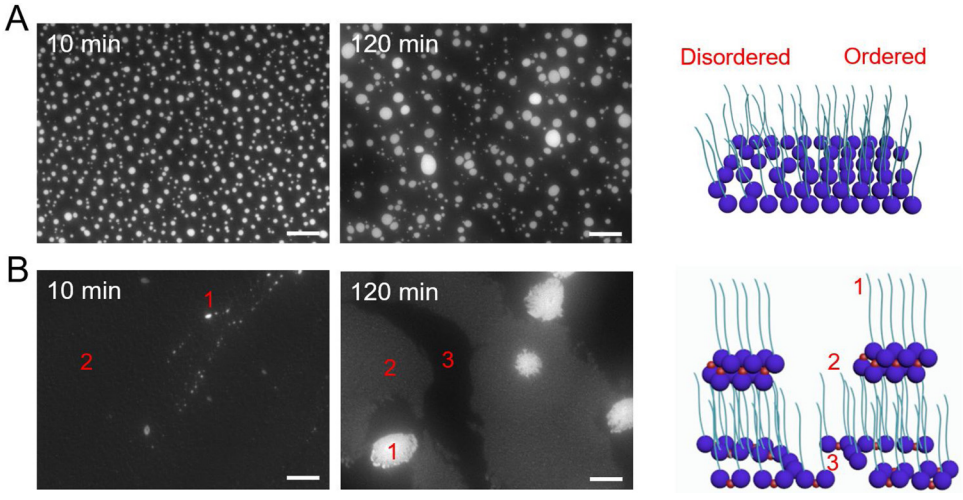

Fig. 1. Topography changes and schematics of the PA films over time on Ca and Ca-free buffers at a constant surface area. (A) Representative topographies of the film at 10 and 120 min after PA was deposited on the Ca-free buffer at the gas-liquid interface. The fluorescent contrast indicated the mixture of disordered (bright) and ordered (dark) domains. (B) Representative topographies of the film at 10 and 120 min after PA was deposited on the Ca buffer at the gas-liquid interface. Three distinct phases with different fluorescent intensities were observed: (1) inverted bilayer domains with the highest fluorescent intensity, (2) a mottled monolayer phases with the intermediate fluorescent intensity, and (3) a uniformly dark gaseous phase as the black surrounding region. The schematics show the possible molecular packing structures of PA molecules on the two buffers. The red dots represent Ca^{2+} ions. The scale bars in all the frames represent 50 μm. The intensity contrast between phases were automatically adjusted to the best contrast. (For interpretation of the references to colour in this figure legend, the reader is referred to the web version of this article).

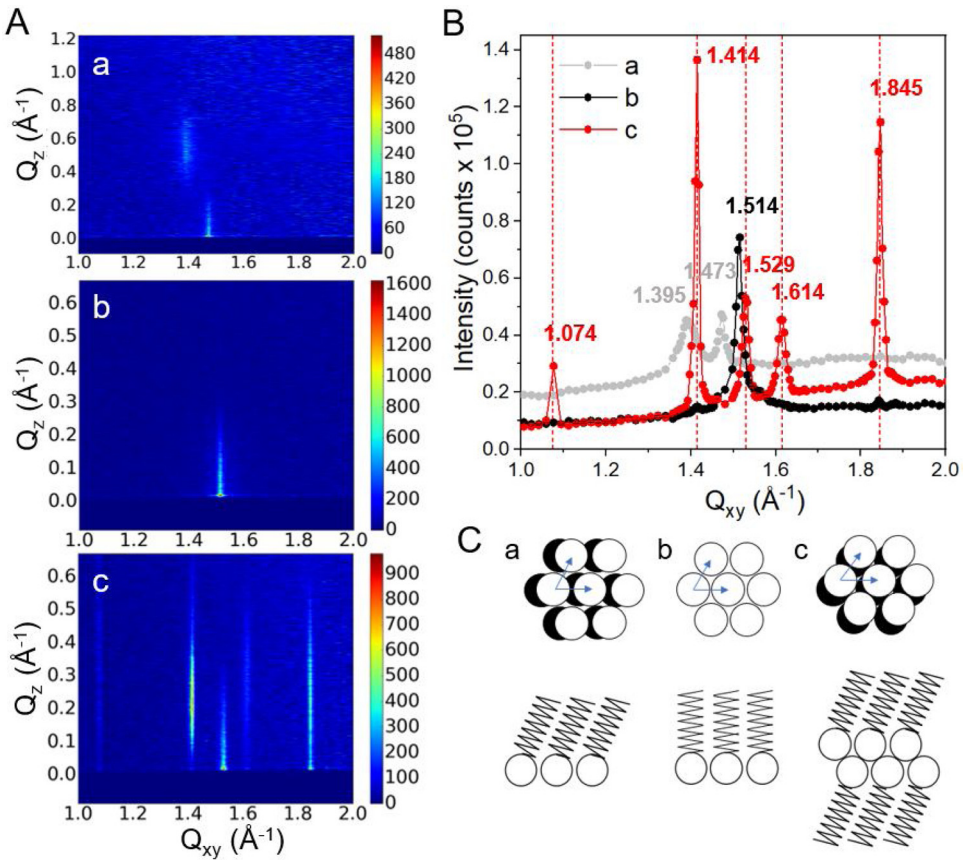

Fig. 2. Molecular organization of the PA films on Ca-free and Ca buffers at a constant surface area. (A) GIXD patterns of the films for (a) 20 min after PA was deposited on the Ca-free buffer, (b) 20 min after PA was deposited on the Ca buffer, and (c) 200 min after PA was deposited on the Ca buffer. (B) Bragg peaks of the films corresponding to Fig. 2A (a) – (c). The vertical dashed lines represent the Bragg peak positions observed 200 min after PA was deposited on the Ca buffer. (C) Schematics of PA molecular packing corresponding to the three conditions of Fig. 2A (a) – (c). The top view is shown in the top row and the side view in the bottom row. (For interpretation of the references to colour in this figure legend, the reader is referred to the web version of this article).

packing structure with a unit area of 19.9 Å^2 (Fig. 2C, schematic b), which is smaller than the unit area of PA molecules on the Ca-free buffer. This is due to the condensing effect of Ca^{2+} on the packing of PA molecules through electrostatic interactions, which was also observed when BA was deposited on buffers containing Cd^{2+} [10].

After 200 min, the Bragg peaks at about 1.41 and 1.84 Å^{-1} became dominant, and three new sharp peaks appeared at 1.074, 1.529, and 1.614 Å^{-1}, while the in-plane peak at 1.514 Å^{-1} was barely discernable (Fig. 2A frame c and Fig. 2B curve c). This new GIXD pattern is similar to that of the highly organized PA-Ca^{2+} superstructures observed at a constant surface pressure. [5,6,26] More specifically, the slow decay along Q_z of the first peak at Q_{xy} = 1.074 Å^{-1} was from the ordered Ca^{2+} layer. The following three Bragg peaks at 1.414 Å^{-1}, 1.529 Å^{-1}, and 1.614 Å^{-1} were scattered from the same organization of PA alkyl tails with an oblique packing structures (Fig. 2C, schematic c), whose unit area was 19.9 Å^2. The last Bragg peak at 1.845 Å^{-1} probably combined the scattering from the ordered Ca layer and alkyl tails, whose organization needs further study. More detailed analysis of the GIXD peaks was described in our previous study. [5]

3.2. Growth kinetics of the inverted bilayer domains

The GIXD measurements indicated that the hexagonal packing of PA molecules was gradually replaced by the PA-Ca^{2+} superstructures at a constant area without any compression of the barrier. The kinetics of this spontaneous transformation into superstructures of PA and Ca^{2+} was further quantified by seven continuous XR measurements over about three hours.

XR results for PA films on the Ca-free buffer again indicated a stable monolayer structure (Fig. 3A). The ED profile obtained from fitting the XR data using a four-box model is displayed in the middle frame of Fig. 3B and the corresponding structural parameters are listed in Table s1. The additional layer below the head group region may represent the accumulated tris molecules around the deprotonated carboxyl groups of the PA molecules.

Different from the stable monolayer organization of the PA film on the Ca-free buffer, a spontaneous collapse of the PA film was observed on the Ca buffer at a constant area. All seven sets of XR data exhibited less intensity decay along the Q_z direction compared to the XR data for the PA film on the Ca-free buffer. This phenomenon became more pronounced over time. In addition, for the last three measurements, the XR curves showed a dip just above the critical angle (Q_z = 0.0217 Å^{-1}). These characteristics suggested an inverted bilayer organization. [37,38] The best fits for the XR data were achieved by using three-phase box models, containing an inverted bilayer, a monolayer, and a gaseous phase. The resulted ED profile and surface coverage are respectively displayed in Figs. 3B and C and the structural parameters are listed in Table s2. The ED profiles of the inverted bilayer were similar for all seven measurements, except that the thickness of the deficit layers (regions where the ED was close to 0) between the inverted bilayer and the subphase increased over time. Self-assembly of the inverted bilayer packing structures is driven by electrostatic interactions of the deprotonated PA with Ca^{2+} and the hydrophobic interactions of the alkyl tails that overcome the entropy decrease. Consequently, the inverted bilayer domains are very rigid, which is consistent with the low roughness obtained from fitting the XR data. Over time, the roughness of the monolayer also decreased, suggesting a more rigid packing structure. Compared to the PA monolayer on the Ca-free buffer, the monolayer domains of the PA film on the Ca buffer were denser and thicker, demonstrating the condensing effect of Ca^{2+} on PA molecular packing.

The spontaneous transition from 2-D to 3-D structures was quantified by analyzing the surface coverage of the three different domains (Fig. 3C). The surface coverage of the inverted bilayer domains slowly increased over time, accompanied by a gaseous phase that emerged and grew to more than 20 % of the surface coverage. At the same time, the

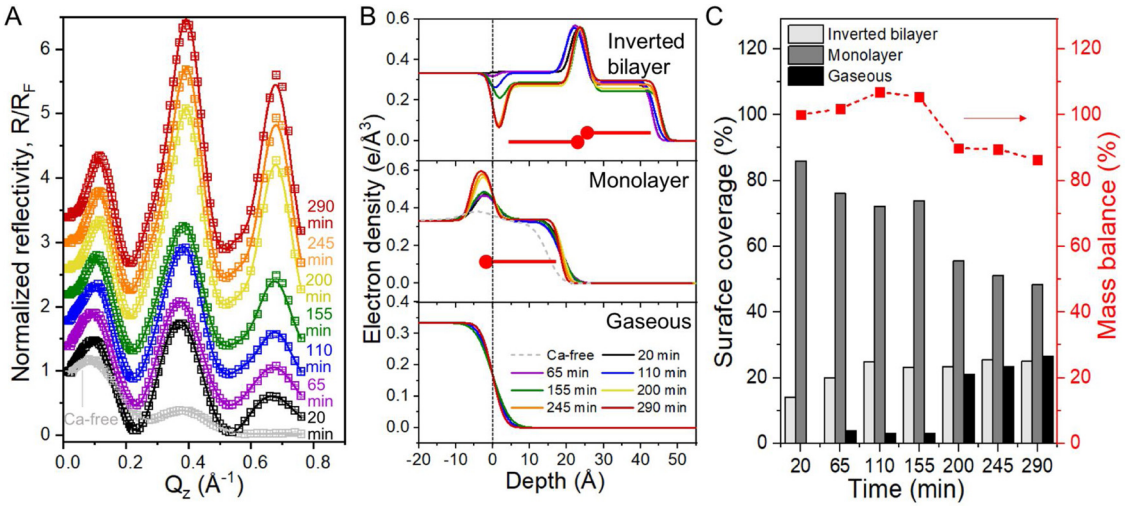

Fig. 3. Reorganization kinetics of the PA film on the Ca buffer at a constant surface area. (A) Normalized XR data obtained from seven continuous measurements on the PA films on the Ca buffer. The solid lines show best fits of the data. The data are offset for clarity. Time was counted from the instant PA was deposited on the buffers. The normalized XR data and their best fit for the PA film on the Ca-free buffer are also included for comparison and displayed as gray dots and a gray solid line, respectively. (B) ED profiles for the inverted bilayer, monolayer, and gaseous phases obtained from fitting the XR data. Same color scales were used as Fig. 3A. The vertical dashed line at the zero depth of the ED profiles indicates the aqueous surface position. The red schematic molecules represent PA packing structures across the interface. (C) Surface coverage of the inverted bilayer, monolayer, and gaseous phases and mass balance of PA molecules overtime. (For interpretation of the references to colour in this figure legend, the reader is referred to the web version of this article).

surface coverage of the monolayer domains decreased by about 42 %. Mass balance of PA molecules over time was analyzed and presented in Fig. 3C (the red dotted line). This was calculated by assuming that the amounts of PA in the bilayer doubled those in the monolayer at the same surface coverage and the amount of PA in the gaseous phase was negligible. More specifically, the average area per molecule is about 20 $Å^2$ for the monolayer domain from the initial isotherm measurements and 10 $Å^2$ for the bilayer domain by assumption. Mass balance of PA molecules approximately maintained throughout the XR measurements.

Electrostatic interactions between the deprotonated COO^- of PA and the Ca^{2+}, together with the hydrophobic interactions of the alkyl tails, overcome the entropy lose and play a key role in stabilizing the PA bilayers on the aqueous phase. The pKa value of monomeric PA in the bulk is about 4.8, but the pKa values for fatty acid aggregates scatter widely in literature, ranging from about 6–9. [39–41] Gershevitz and Sukenik observed two pKa values at about 4.9 and 9.3 for the siloxane anchored fatty acid monolayers in water [41]. At a near-neutral pH, PA deprotonation and strong binding of COO- with Ca^{2+} were characterized by Tang et al. using vibrational sum frequency generation spectroscopy (VSFGS). [42] Therefore, it is reasonable to consider that a significant amount of PA in the films were deprotonated with the presence of Ca^{2+} at pH 7.4 under our experimental conditions.

The non-linear growth kinetics may have been resulted from complicated coupling effects of domain merging and molecular transport from the monolayer to the bilayer domains. Data with a higher temporal resolution may be necessary for developing the theory. In this study, we employed MD simulations to reveal a few important steps of the nucleation and growth processes. To simulate the initial nucleation, an MD run was conducted on a densely packed monolayer of PA with Ca^{2+} at a unit area of 12.6 $Å^2$, which is oversaturated at the interface. When the damping coefficient was lowered to 1 ps^{-1} after equilibration for 1 ns at a high damping coefficient of 5 ps^{-1}, the monolayer immediately became corrugated (at ~0.05 ns). Prior to full corrugation, small bundles of PA molecules were ejected above and below the monolayer simultaneously (Fig. 4A and Video in Supplemental Information 2). This ejection preceding corrugation was similar to the finding of a previous study on the monolayer collapse of deprotonated arachidonic acid (AA) on a Ca^{2+} buffer under a constant pressure. [43] Following the corrugation, the ejected PA molecules and Ca^{2+} then reorganized and formed the inverted bilayer nuclei of PA-Ca^{2+} complexes at the interface (Fig. 4A). Due to computational limitations, the initial density of the PA molecules in the MD simulation was set higher than that in the experimental conditions in order to accelerate the nucleation process without losing physical insights. Nonetheless, the MD results suggest that spontaneous nucleation of PA-Ca^{2+} inverted bilayers probably occurs in densely packed PA molecules at the interface during or shortly after their deposition through this “corrugation–ejection–complex formation” mechanism.

To simulate the nuclei growth, an MD run was conducted using a model containing a monolayer domain adjacent to an inverted bilayer domain at the gas-liquid interface (Fig. 4B). The initial PA densities in the simulation were set to be similar to the experimental conditions. During 55.2 ns of equilibration, the PA and Ca^{2+} in the inverted bilayer became more tightly packed and organized than those in the monolayer. Moreover, PA and Ca^{2+} in the monolayer continuously migrated into the inverted bilayer (Video in Supplemental Information 3). During this migration, PA had a strong interaction with Ca^{2+} and rotated around it. By this way, the PA-Ca^{2+} complex kept integrating into the inverted bilayer structure. In addition, exchanges of PA molecules occurred between the top and bottom leaflets in the inverted bilayer domain (Video in Supplemental Information 3), which further supports the possibility of frequent rotation and migration of the PA-Ca^{2+} complexes. The molecular transport of PA and Ca^{2+}, named as “bonding–migration–rotation”, may be the main mechanism for the changes in surface coverage of the three phases as observed in the experiments.

4. Conclusions

To the best of our knowledge, the present study is the first to report the spontaneous collapse (2D to 3D transition) of an SFA film at a constant surface area. The study examined the interfacial reorganization of PA films on a weak alkaline buffer with and without Ca^{2+}. Results showed that Ca^{2+} played an essential role in the reorganization. PA molecules formed a stable monolayer with an NN- tilted lateral packing structure on the Ca-free buffer. In contrast, due to the strong electrostatic interaction of deprotonated PA head groups with Ca^{2+} and the hydrophobic effects of alkyl tails, the PA molecules and Ca^{2+}

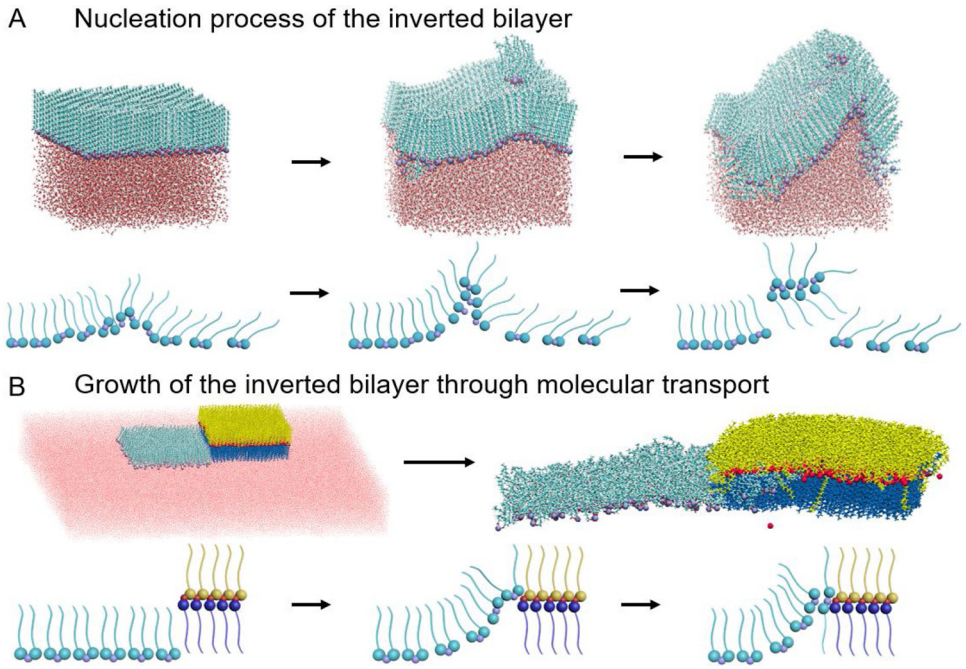

Fig. 4. MD simulations and schematics of the nucleation and growth processes of the inverted bilayer superstructures of PA and Ca^{2+} at a constant surface area at the gas-liquid interface. (A) Corrugation and ejection of the PA molecules indicated by the MD simulation, which may be the main mechanism involved in the formation of inverted bilayer nuclei. Ejection was observed after 2 ns of equilibration. (B) Molecular transport of PA and Ca^{2+} from the monolayer domain to the co-existing inverted bilayer domain. For all the frames, a consistent color code was used: light blue is for the initial PA monolayer; yellow is for the initial top leaflet of the PA inverted bilayer; dark blue is for the initial bottom leaflet of the PA inverted bilayer; purple spheres are Ca^{2+} ions initially placed in solution beneath the PA monolayer; red spheres are Ca^{2+} ions initially placed between the top and bottom PA leaflets of the inverted bilayer; and small red dots underneath are water molecules. (For interpretation of the references to colour in this figure legend, the reader is referred to the web version of this article).

cations spontaneously transformed from a primary monolayer structure to a highly heterogeneous mixture of monolayer, inverted bilayer, and gaseous phases. This spontaneous collapse of the PA-Ca^{2+} film occurred through a two-step mechanism involving nucleation and nuclei growth of the inverted bilayer domains. Bilayer domain nucleation may proceed through "corrugation–ejection–complex formation," and the growth of the bilayer domain is contributed by the continuous molecular transport of PA and Ca^{2+} from the monolayer domain to the inverted bilayer domains. The study of the spontaneous collapse of SFA films with divalent cations sheds light on their roles in bioprocesses and provides a foundation for designing related biomimetic systems.

CRediT authorship contribution statement

Pin Zhang: Data curation, Formal analysis, Investigation, Writing - original draft, Writing - review & editing. **Tiep Pham:** Data curation, Investigation. **Xin Zheng:** Software. **Chang Liu:** Investigation. **Paola Leon Plata:** Investigation. **Petr Král:** Software. **Wei Bu:** Methodology, Resources. **Binhua Lin:** Project administration, Resources. **Ying Liu:** Supervision, Investigation, Funding acquisition, Writing - review & editing.

Declaration of Competing Interest

The authors declare that they have no known competing financial interests or personal relationships that could have appeared to influence the work reported in this paper.

Acknowledgments

The study is partially supported by the NSF Nanomanufacturing Program (NSF CAREER#1350731). NSF's ChemMatCARS Sector 15 is supported by the Divisions of Chemistry (CHE) and Materials Research (DMR), National Science Foundation, under grant number NSF/CHE-1834750. Use of the Advanced Photon Source, an Office of Science User Facility operated for the U.S. Department of Energy (DOE) Office of Science by Argonne National Laboratory, was supported by the U.S. DOE under Contract No. DE-AC02-06CH11357. The authors are grateful to Professor Ursula Perez-Salas and Professor Mark L. Schlossman for access to their laboratories and much helpful advice.

Appendix A. Supplementary data

Supplementary material related to this article can be found, in the online version, at doi:https://doi.org/10.1016/j.colsurfb.2020.111100.

References

[1] P.C. Calder, Functional roles of fatty acids and their effects on human health, J. Parenter. Enter. Nutr. 39 (2015) 18S–32S.
[2] S. Weiner, L. Addadi, Crystallization pathways in Biomineralization, Annu. Rev. Mater. Res. 41 (2011) 21–40.
[3] F. Leveiller, D. Jacquemain, M. Lahav, L. Leiserowitz, M. Deutsch, K. kjaer, J. Als-Nielsen, Crystallinity of the double layer of cadmium arachidate films at the water surface, Science 252 (1991) 1532–1536.
[4] S. Cantin, M.-C. Fauré, F. Perrot, M. Goldmann, Structure and kinetics of fatty acid langmuir monolayers on zinc salt solutions, J. Phys. Chem. B 117 (2013) 16275–16282.
[5] P. Zhang, V. Villanueva, J. Kalkowski, C. Liu, A.J. Donovan, W. Bu, M.L. Schlossman, B. Lin, Y. Liu, Molecular interactions of phospholipid monolayers with a model phospholipase, Soft Matter 15 (2019) 4068–4077.
[6] P. Zhang, V. Villanueva, J. Kalkowski, C. Liu, T. Pham, U. Perez-Salas, W. Bu, B. Lin, Y. Liu, Polyunsaturated phospholipid modified membrane degradation catalyzed by a secreted phospholipase A2, Langmuir 35 (2019) 11643–11650.
[7] J. Kmetko, A. Datta, G. Evmenenko, P. Dutta, The effects of divalent ions on Langmuir Monolayer and subphase structure: a grazing-incidence diffraction and Bragg rod study, J. Phys. Chem. B 105 (2001) 10818–10825.
[8] K. Das, B.K. Sah, S. Kundu, Cation-induced monolayer collapse at lower surface pressure follows specific headgroup percolation, Phys. Rev. E 95 (2017) 022804.
[9] K. Das, S. Kundu, Subphase pH induced monolayer to multilayer collapse of fatty acid Salt Langmuir monolayer at lower surface pressure, Colloids Surf. A Physicochem. Eng. Asp. 492 (2016) 54–61.
[10] S. Cantin, J. Pignat, F. Perrot, P. Fontaine, M. Goldmann, Observation of a two-step mechanism in the formation of a superstructure of cadmium-behenic acid Langmuir monolayer: evidence of an intermediate structure, Phys. Rev. E 70 (2004) 050601.
[11] M.D. Phan, J. Lee, K. Shin, Collapsed states of langmuir monolayers, J. Oleo Sci. 65 (2016) 385–397.
[12] S. Kundu, A. Datta, S. Hazra, Effect of metal ions on monolayer collapses, Langmuir 21 (2005) 5894–5900.
[13] W. Bu, D. Vaknin, Bilayer and trilayer crystalline formation by collapsing behenic acid monolayers at Gas/Aqueous interfaces, Langmuir 24 (2008) 441–447.
[14] B.A. Capistran, G.J. Blanchard, Effects of Cu(II) on the formation and orientation of an arachidic acid langmuir–Blodgett film, Langmuir 35 (2019) 3346–3353.
[15] H.E. Ries, Stable ridges in a collapsing monolayer, Nature 281 (1979) 287–289.
[16] A. Gopal, K.Y.C. Lee, Morphology and Collapse Transitions in Binary Phospholipid Monolayers, J. Phys. Chem. B 105 (2001) 10348–10354.
[17] K.Y.C. Lee, Collapse mechanisms of langmuir monolayers, Annu. Rev. Phys. Chem. 59 (2008) 771–791.
[18] A. Datta, J. Kmetko, C.J. Yu, A.G. Richter, K.S. Chung, J.M. Bai, P. Dutta, pH-dependent appearance of chiral structure in a langmuir monolayer, J. Phys. Chem. B 104 (2000) 5797–5802.

[19] V. Dupres, S. Cantin, F. Benhabib, F. Perrot, P. Fontaine, M. Goldmann, J. Daillant, O. Konovalov, Superlattice formation in fatty acid monolayers on a divalent ion subphase: role of chain length, temperature, and subphase concentration, Langmuir 19 (2003) 10808–10815.
[20] F. Leveiller, C. Boehm, D. Jacquemain, H. Moehwald, L. Leiserowitz, K. Kjaer, J. Als-Nielsen, Two-dimensional crystal structure of cadmium arachidate studied by synchrotron X-ray diffraction and reflectivity, Langmuir 10 (1994) 819–829.
[21] A. El Haitami, M. Goldmann, P. Fontaine, M.-C. Fauré, S. Cantin, Inorganic mixed phase templated by a fatty acid monolayer at the air–water interface: the Mn and Mg case, J. Chem. Soc. Faraday Trans. 20 (2018) 6629–6637.
[22] M.I. Boyanov, J. Kmetko, T. Shibata, A. Datta, P. Dutta, B.A. Bunker, Mechanism of Pb adsorption to fatty acid langmuir monolayers studied by X-ray absorption fine structure spectroscopy, J. Phys. Chem. B 107 (2003) 9780–9788.
[23] D. Vollhardt, U. Retter, Nucleation in insoluble monolayers. 3. Overlapping effect of the growing centers, Langmuir 8 (1992) 309–312.
[24] D. Vollhardt, Nucleation in monolayers, Adv. Colloid Interface Sci. 123-126 (2006) 173–188.
[25] M.C. Shih, T.M. Bohanon, J.M. Mikrut, P. Zschack, P. Dutta, Pressure and pH dependence of the structure of a fatty acid monolayer with calcium ions in the subphase, J. Chem. Phys. 96 (1992) 1556–1559.
[26] P. Zhang, T. Pham, C. Liu, P.L. Plata, J. Kalkowski, G. Cheng, W. Bu, B. Lin, Y. Liu, Effects of polyethylene glycol brushes on lipid interfacial organization and enzyme-catalyzed degradation, Langmuir (2020).
[27] A.M. Tikhonov, S.V. Pingali, M.L. Schlossman, Molecular ordering and phase transitions in alkanol monolayers at the water–hexane interface, J. Chem. Phys. 120 (2004) 11822–11838.
[28] L.G. Parratt, Surface studies of solids by total reflection of X-rays, Phys. Rev. 95 (1954) 359–369.
[29] J.C. Phillips, R. Braun, W. Wang, J. Gumbart, E. Tajkhorshid, E. Villa, C. Chipot, R.D. Skeel, L. Kalé, K. Schulten, Scalable molecular dynamics with NAMD, J. Comput. Chem. 26 (2005) 1781–1802.
[30] N. Foloppe, J. MacKerell, D. Alexander, All-atom empirical force field for nucleic acids: I. Parameter optimization based on small molecule and condensed phase macromolecular target data, J. Comput. Chem. 21 (2000) 86–104.
[31] A.D. MacKerell Jr., N.K. Banavali, All-atom empirical force field for nucleic acids: II. Application to molecular dynamics simulations of DNA and RNA in solution, J. Comput. Chem. 21 (2000) 105–120.
[32] W.L. Jorgensen, J. Chandrasekhar, J.D. Madura, R.W. Impey, M.L. Klein, Comparison of simple potential functions for simulating liquid water, J. Chem. Phys. 79 (1983) 926–935.
[33] K. Vanommeslaeghe, E. Hatcher, C. Acharya, S. Kundu, S. Zhong, J. Shim, E. Darian, O. Guvench, P. Lopes, I. Vorobyov, A.D. Mackerell Jr, CHARMM general force field: a force field for drug-like molecules compatible with the CHARMM all-atom additive biological force fields, J. Comput. Chem. 31 (2010) 671–690.
[34] A.D. MacKerell, D. Bashford, M. Bellott, R.L. Dunbrack, J.D. Evanseck, M.J. Field, S. Fischer, J. Gao, H. Guo, S. Ha, D. Joseph-McCarthy, L. Kuchnir, K. Kuczera, F.T.K. Lau, C. Mattos, S. Michnick, T. Ngo, D.T. Nguyen, B. Prodhom, W.E. Reiher, B. Roux, M. Schlenkrich, J.C. Smith, R. Stote, J. Straub, M. Watanabe, J. Wiórkiewicz-Kuczera, D. Yin, M. Karplus, All-atom empirical potential for molecular modeling and dynamics studies of proteins, J. Phys. Chem. B 102 (1998) 3586–3616.
[35] T. Darden, D. York, L. Pedersen, Particle mesh Ewald: an N·log(N) method for Ewald sums in large systems, J. Chem. Phys. 98 (1993) 10089–10092.
[36] K.Y.C. Lee, A. Gopal, A. von Nahmen, J.A. Zasadzinski, J. Majewski, G.S. Smith, P.B. Howes, K. Kjaer, Influence of palmitic acid and hexadecanol on the phase transition temperature and molecular packing of dipalmitoylphosphatidyl-choline monolayers at the air–water interface, J. Chem. Phys. 116 (2001) 774–783.
[37] W. Bu, H. Yu, G. Luo, M.K. Bera, B. Hou, A.W. Schuman, B. Lin, M. Meron, I. Kuzmenko, M.R. Antonio, L. Soderholm, M.L. Schlossman, Observation of a rare earth ion–Extractant complex arrested at the oil–Water interface during solvent extraction, J. Phys. Chem. B 118 (2014) 10662–10674.
[38] D. Vaknin, W. Bu, S.K. Satija, A. Travesset, Ordering by collapse: formation of bilayer and trilayer crystals by folding langmuir monolayers, Langmuir 23 (2007) 1888–1897.
[39] M. Egret-Charlier, A. Sanson, M. Ptak, O. Bouloussa, Ionization of fatty acids at the lipid—water interface, FEBS Lett. 89 (1978) 313–316.
[40] A.A. Pashkovskaya, M. Vazdar, L. Zimmermann, O. Jovanovic, P. Pohl, E.E. Pohl, Mechanism of long-chain free fatty acid protonation at the membrane-water interface, Biophys. J. 114 (2018) 2142–2151.
[41] O. Gershevitz, C.N. Sukenik, In situ FTIR-ATR analysis and titration of carboxylic acid-terminated SAMs, J. Am. Chem. Soc. 126 (2004) 482–483.
[42] C.Y. Tang, Z. Huang, H.C. Allen, Binding of $Mg2+$ and $Ca2+$ to palmitic acid and deprotonation of the COOH headgroup studied by vibrational sum frequency generation spectroscopy, J. Phys. Chem. B 114 (2010) 17068–17076.
[43] C.D. Lorenz, A. Travesset, Atomistic simulations of langmuir monolayer collapse, Langmuir 22 (2006) 10016–10024.